Facets coupling of BiOBr-g-C$_3$N$_4$ composite photocatalyst for enhanced visible-light-driven photocatalytic activity

Liqun Ye [a,b], Jinyan Liu [a], Zhuo Jiang [a], Tianyou Peng [a], Ling Zan [a,*]

[a] College of Chemistry and Molecular Science, Wuhan University, Wuhan 430072, People's Republic of China
[b] College of Chemistry and Pharmaceutical Engineering, Nanyang Normal University, Nanyang 473061, People's Republic of China

ABSTRACT

BiOBr-g-C$_3$N$_4$ inorganic–organic composite photocatalysts were synthesized by a one-step chemical bath method at low temperature and characterized by X-ray diffraction patterns (XRD), Fourier transform infrared (FT-IR), thermo gravimetric (TG), X-ray photoelectron spectroscopy (XPS), transmission electron microscopy (TEM), high-resolution transmission electron microscopy (HRTEM) and UV–vis diffuse reflectance spectra (DRS). The BiOBr-g-C$_3$N$_4$ composite showed much higher visible-light-driven (VLD) photocatalytic activity than pure g-C$_3$N$_4$ and BiOBr for rhodamine B (RhB) degradation. The photocatalytic mechanism analysis revealed that the interreaction between BiOBr and g-C$_3$N$_4$ is a kind of facet coupling between BiOBr-{0 0 1} and g-C$_3$N$_4$-{0 0 2}. The active species trapping and quantification experiments indicated that the photoinduced charges transfer between these facets resulted in the efficient charge separation.

Crown Copyright © 2013 Published by Elsevier B.V. All rights reserved.

1. Introduction

Semiconductor photocatalysis technique is a "green" method to completely eliminate most kinds of environmental contaminations [1]. The development of visible-light-driven (VLD) photocatalysts has been done by more and more researchers [2]. Recently, BiOX (X = Cl, Br, I) were reported as an efficient photocatalysts [3–11]. BiOX have indirect-transition band-gap and layered structure. The indirect-transition band-gap of BiOX result in that the excited electron has to travel a certain k-space distance to be emitted to the valence band (VB) which reduces the recombination probability of the excited electron and the hole [12–14]. On the other hand, the layered structure provides a large enough space to polarize the related atoms and orbitals, and then induce the presence of internal static electric fields perpendicular to the [Bi$_2$O$_2$] slabs and halogen anionic slabs in BiOX [12–14]. At end, effective separation of the photoinduced electron–hole pairs along the [0 0 1] direction can be displayed. So, BiOX display high photocatalytic activity. Among the BiOX photocatalysts, BiOBr shows the appropriate band-gap (2.75 eV) which results in the best photocatalytic oxidation and reduction activity under visible light irradiation. Now, BiOBr has been widely used in photocatalytic

degradation (PCD) of dyes, nitrogen oxide and microcystin-LR [9–11,15,16].

Graphitic carbon nitrides (g-C$_3$N$_4$) are recognized as the most stable allotrope of carbon nitride and have an optical band gap of 2.7 eV [17,18]. It can be synthesized from a simple precursor via a series of polycondensation reactions without any metal involvement [17–20]. Due to its high nitrogen content and facile synthesis procedure, g-C$_3$N$_4$ may provide more active reaction sites than other N-carbon materials. Recently, Wang et al. firstly reported that g-C$_3$N$_4$ can be used for hydrogen or oxygen production from water splitting under visible light irradiation [17]. But, many followed reports showed that its photocatalytic activity is very low. In order to improve its photocatalytic activity, the g-C$_3$N$_4$ composite photocatalysts (TaON-g-C$_3$N$_4$, [21] TiO$_2$-g-C$_3$N$_4$, [22,23] ZnO-g-C$_3$N$_4$, [24,25] Bi$_2$WO$_6$-g-C$_3$N$_4$, [26,27] SrTiO$_3$-g-C$_3$N$_4$, [28]) were prepared and used for the photodegradation of azo dyes. However, to the best of our knowledge, there are few reports to study coupling mode of g-C$_3$N$_4$ and inorganic composite photocatalyst. And the photocatalytic mechanism of those inorganic–organic composite photocatalyst remains far from clear.

In this paper, the novel BiOBr-g-C$_3$N$_4$ composite photocatalyst was prepared. The aim was to further improve the VLD photocatalytic activity of BiOBr and g-C$_3$N$_4$. The results showed that the BiOBr-g-C$_3$N$_4$ photocatalyst had a remarkably enhanced RhB photodegradation activity under visible light irradiation comparing with pure BiOBr and g-C$_3$N$_4$. The mechanism for the degradation of RhB over the BiOBr-g-C$_3$N$_4$ also was discussed.

---

* Corresponding author.
E-mail address: irlab@whu.edu.cn (L. Zan).

2. Experimental

2.1. Materials

Thiourea (Tu, analytical pure) was bought from Tianjin Taixing Chemical Reagent Factory. $Bi(NO_3)_3 \cdot 5H_2O$, terephthalic acid (TA), p-benzoquinone (BQ), isopropanol (IPA), triethanolamine (TEOA), nitroblue tetrazolium (NBT), cetyltrimethylammonium bromide (CTAB) and ethanol were analytical pure and from Sinopharm Chemical Reagent Co., Ltd. Rhodamine B (RhB) was analytical pure and used without further purification.

2.2. Synthesis

g-C_3N_4 was synthesized by annealing Tu at 550 °C for 3 h with the heating rate of 5 °C min^{-1} [29,30]. The BiOBr-g-C_3N_4 was synthesized as follows: 0.12 g $Bi(NO_3)_3 \cdot 5H_2O$ was dissolved in 50 mL deionized water (pH 3 by adding HNO_3). 0.064 g g-C_3N_4 was suspensed in 50 mL CTAB solution (8×10^{-3} mol/L). Then $Bi(NO_3)_3 \cdot 5H_2O$ solution were dropped in g-C_3N_4 suspension. The mixture was stirred and heated in water bath at 80 °C for 3 h. After completion of the reaction, the suspension was filtered. The precipitate was washed by absolute ethanol and deionized water for three times and transferred to oven to dry at 80 °C for 24 h. The obtained BiOBr-g-C_3N_4 contains 50% BiOBr and 50% g-C_3N_4 which was proved by TG (Fig. S1), and is in agreement with above feed ratio. For comparison, pure BiOBr and other feed ratio BiOBr-g-C_3N_4 samples were synthesized using the similar processes.

2.3. Characterization

X-ray diffraction patterns (XRD) of the samples recorded at room temperature, by a Bruker D8 advance X-ray diffractometer using Cu Kα radiation and 2θ scan rate of 6 min^{-1}. Diffraction patterns were taken over the 2θ range 8–70°. The thermo gravimetric analyses (TGA) of the precursors were performed by using an NETZSCH STA 449C TGA thermal analyzer with a heating rate of 10 °C min^{-1} and the range of temperature from 30 to 750 °C in air atmosphere. The infrared spectra were obtained on a Nicolet Magna-IR 550 Fourier transform infrared (FT-IR) spectrometer and KBr as the reference sample within wavelength range of 400–4000 cm^{-1}. X-ray photo-electron spectroscopy (XPS) measurements were carried out by a VG Multilab 2000 spectrometer (Thermo Electron Corporation) with an Mg Kα X-ray source, and the spectra calibrated to the C 1s peak at 284.6 eV. Transmission electron microscopy (TEM), selected area electron diffraction (SAED) pattern and high-resolution transmission electron microscopy (HRTEM) image was obtained by a JEOL JEM-2000 (RH) Field Emission Electron Microscope with operating at an accelerating voltage of 200 kV. UV–vis diffuse reflectance spectra (DRS) were obtained using a Shimadzu UV-3600 spectrometer by using $BaSO_4$ as a reference.

2.4. Photocatalytic activity test

The photocatalytic activities were evaluated by the degradation of RhB under visible light ($\lambda \geq 400$ nm) irradiation. The visible light was obtained by a 500 W high pressure xenon lamp with a 400 nm (or 500 nm) cut off filter to ensure the needed irradiation light. The xenon lamp was bought from Changzhou Yuyu Electro-Optical Device Co., Ltd. China. Typical photocatalytic degradation process is arranged in this way: 50 mL aqueous suspensions of 10 mg/L RhB was placed in a quartz glass beaker, and then 10 mg photocatalysts were added. Prior to irradiation, the suspensions were sonicated for 10 min and then magnetically stirred in dark for 30 min to get desorption–adsorption equilibrium. The suspensions were kept under constant air-equilibrated conditions during irradiation. A
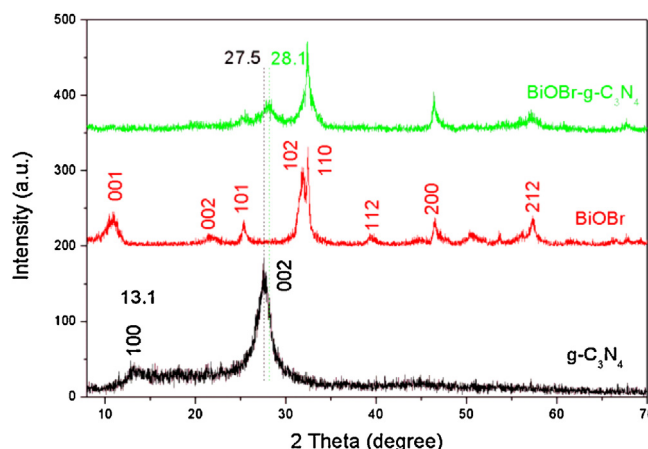

Fig. 1. (a) XRD patterns of precursors; and (b) XRD patterns of BiOCl samples.

magnetic stirrer was employed for continuous mixing. At certain time intervals, 4 mL suspensions were sampled and centrifuged by TGL-16G centrifuge (Shanghai Anting Scientific Instrument Factory, China) at 10,000 rpm for 15 min to remove the particles. The upper clear liquid was analyzed by recording the maximum absorption band (553 nm for RhB) and UV–vis spectra of dyes using a Shimadzu UV-3600 spectrophotometer.

2.5. Active species trapping and $O_2^{\bullet-}$ and $^{\bullet}OH$ quantification experiments

For detecting the active species during photocatalytic reactivity, hydroxyl radicals ($^{\bullet}OH$), superoxide radical ($O_2^{\bullet-}$) and holes (h+) were investigated by adding 1.0 mM IPA (a quencher of $^{\bullet}OH$), 1 mM BQ (a quencher of $O_2^{\bullet-}$) or 1 mM TEOA (a quencher of h+), [6–8] respectively. The method was similar to the former photocatalytic activity test. NBT (2.5×10^{-5} mol/L, exhibiting an absorption maximum at 259 nm) was used to determine the amount of $O_2^{\bullet-}$ generating from BiOBr, g-C_3N_4 and BiOBr-g-C_3N_4 photocatalytic system. The production of $O_2^{\bullet-}$ was quantitatively analyzed by detecting the concentration of NBT with Shimadzu UV-3600 spectrophotometer. The method was similar to the former photocatalytic activity test with NBT replacing the RhB. TA (5×10^{-4} M in a 2×10^{-3} M NaOH solution), which reacts readily with $^{\bullet}OH$ to produce a highly fluorescent product, 2-hydroxyterephthalic acid, was employed as a probe molecule to determine the amount of $^{\bullet}OH$ generating from BiOBr, g-C_3N_4 and BiOBr-g-C_3N_4. The production of $^{\bullet}OH$ was quantitatively analyzed by detecting the concentration of 2-hydroxyterephthalic acid (fluorescence peak at about 425 nm by excitation with the wavelength of 315 nm) with Shimadzu spectrofluorophotometer (RF-5301pc) after centrifugation. The method was similar to the former photocatalytic activity test with TA replacing the RhB.

3. Results and discussion

3.1. Facets coupling

Fig. 1 shows the XRD patterns of BiOBr, g-C_3N_4 and BiOBr-g-C_3N_4. The XRD peaks of the pure BiOBr were in good agreement with the tetragonal phase of BiOBr (JCPDS 73-2061) [9–11,15,16]. For pure g-C_3N_4, the strongest XRD peak at 27.5, corresponding to 0.326 nm, can be indexed as (0 0 2) diffraction plane (JCPDS 87-1526). It is due to the stacking distance of the conjugated aromatic system, as in graphene oxide. Another pronounced additional peak is found at 13.1, corresponding to a distance $d = 0.675$ nm. This distance is only slightly below the size of one tris-s-triazine unit (ca.
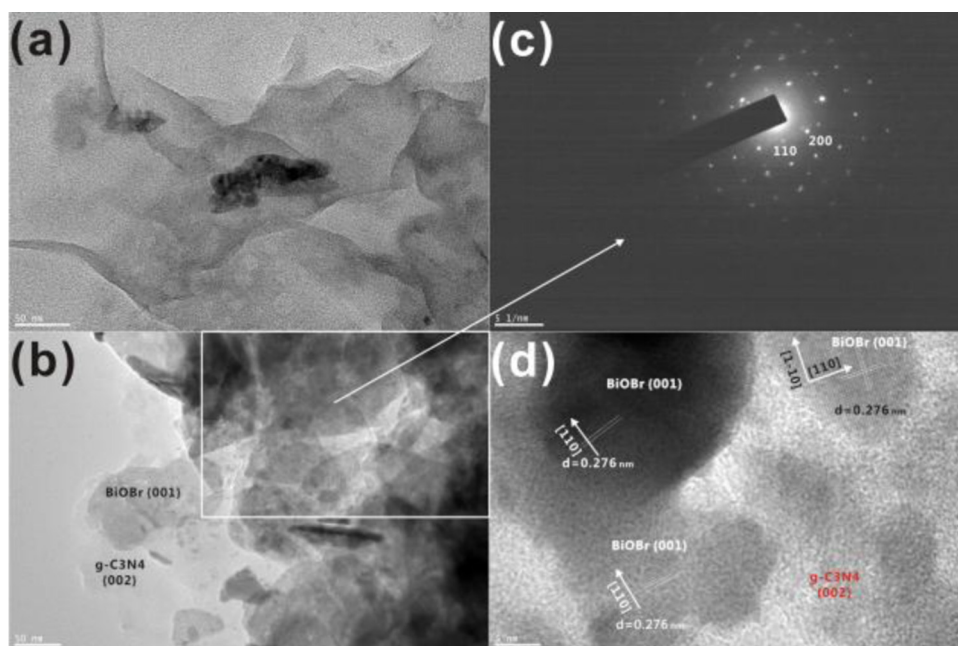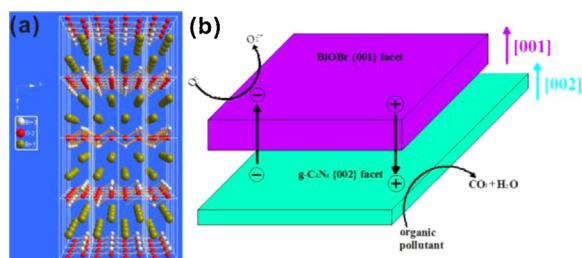
Fig. 2. (a) TEM image of g-C_3N_4; (b) TEM image of BiOBr-g-C_3N_4; (c) SAED pattern of the range in Fig. 2b; and (d) HRTEM image BiOBr-g-C_3N_4.

0.73 nm). Based on the electron microscopy evidence, the peak at 13.1 relates to an in-plane structural packing motif, such as the hole-to-hole distance of the nitride pores in the crystal [17,18]. When BiOBr coupled with g-C_3N_4, it can be found that the (0 0 1) and (0 0 2) peaks of BiOBr disappeared and the (0 0 2) peak of g-C_3N_4 shifted to 28.1. It implied that the coupling between BiOBr and g-C_3N_4 may be happened on BiOBr-{0 0 1} facets and g-C_3N_4-{0 0 2} facets. After facet coupling between BiOBr-{0 0 1} and g-C_3N_4-{0 0 2}, the {0 0 1} facets of BiOBr were cover by g-C_3N_4. So, the intensity of (0 0 1) peaks should be decreased. On the other hand, the half band width of (0 0 1) peaks are larger than others, it also accelerate the disappearance of (0 0 1) peaks. So, facet coupling can result in the disappearance of (0 0 1) and (0 0 2) peaks of BiOBr. For confirming the facets coupling between BiOBr-{0 0 1} and g-C_3N_4-{0 0 2}, FT-IR, TEM, SAED, HRTEM and XPS analysis were applied as following.

Fig. 2a shows the TEM image of g-C_3N_4. It can be seen the wrinkle two-dimensional structure. On the basis of the theoretic and previously experimental crystal structure of g-C_3N_4, it can be concluded that the top surface of wrinkle two-dimensional is the {0 0 2} facets of g-C_3N_4 as shown in Scheme 1b. In Fig. 2b, it can found that the BiOBr nanoflakes lie on {0 0 2} facets of g-C_3N_4. On the other hand, SAED pattern (Fig. 2c) and HRTEM (Fig. 2d) proved the top surface of BiOBr is {0 0 1} facets. So, we can deem that the coupling between BiOBr and g-C_3N_4 happened on BiOBr-{0 0 1} facets and g-C_3N_4-{0 0 2} facets.

Fig. 3 displays the FT-IR spectra of BiOBr, g-C_3N_4, and BiOBr-g-C_3N_4. The strong IR absorption bands in pure g-C_3N_4 sample revealed a typical molecular structure of g-C_3N_4 (Fig. S2). The several intense bands in the 1200–1650 cm^{-1} region were corresponding to the typical stretching modes of CN heterocycles [29,30]. The intense band at 810 cm^{-1} represented the out-of-plane breathing vibration characteristic of triazine units [29,30]. For pure BiOBr, 519 cm^{-1} is assigned as the symmetric stretching vibration peak of the Bi—O band in the BiOBr structure [13]. When BiOBr coupled with g-C_3N_4, it can be found that the stretching modes of CN heterocycles shifted about 5 cm^{-1}. It also indicated that BiOBr coupled with CN heterocycles, namely {0 0 2} facets of g-C_3N_4.

XPS is an advantaged analytical method to confirm coupling mode among atoms. The former TEM, SAED, HRTEM and FT-IR results displayed the coupling happened between g-C_3N_4-{0 0 2} and BiOBr-{0 0 1} facets, but how did the coupling happen in atoms level? Fig. 4a shows the C1s spectra of g-C_3N_4 and BiOBr-g-C_3N_4. The first C peak at 288.01 eV was identified as sp2-bonded carbon (N—C=N), and the second at 284.6 eV was corresponded to graphitic
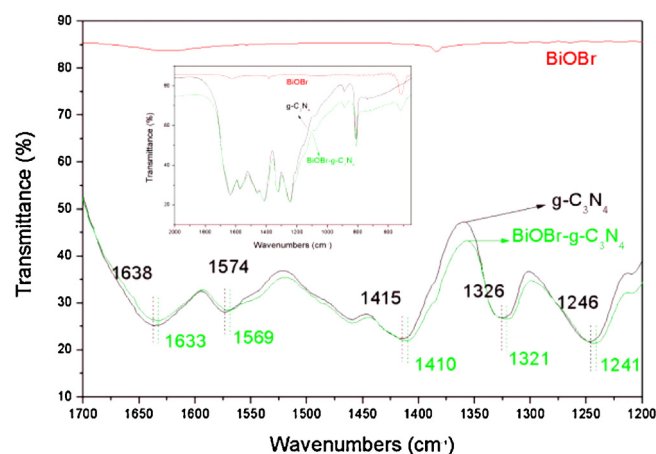

Scheme 1. (a) Crystal structure of BiOBr; and (b) coupling Model of BiOBr-g-C_3N_4.

Fig. 3. FT-IR spectra of BiOBr, g-C_3N_4, and BiOBr-g-C_3N_4. The inset Fig. is the lager range FT-IR spectra with 400–2000 cm^{-1}.

Fig. 4. XPS spectra of the g-C$_3$N$_4$, BiOBr and BiOBr-g-C$_3$N$_4$. (a) C1s; (b) N1s; and (c) O1s.

Fig. 5. UV–vis diffuse reflectance spectra of BiOBr, g-C$_3$N$_4$ and BiOBr-g-C$_3$N$_4$; and the UV–vis absorption spectra of RhB with 10 mg/L.

On the other hand, BiOBr crystal structure (Scheme 1a) showed that the {0 0 1} facets of BiOBr mainly contains terminal O atoms. So, the coupling atoms of BiOBr may be O atoms. The O1s spectra of BiOBr and BiOBr-g-C$_3$N$_4$ were shown in Fig. 4c. For pure BiOBr, 529.5 and 532.0 eV was attributed to crystal lattice O atoms (Bi—O) and surface OH, respectively [11]. The facets coupling results in a higher binding energy of crystal lattice O at 530.0 eV which proved the coupling happened at {0 0 2} facet (O atoms) for BiOBr. The non-change of chemistry shift of Bi3d and Br3p (Fig. S3) also can support it.

3.2. Photocatalytic activity

A comparison of the UV–vis DRS spectra of BiOBr, g-C$_3$N$_4$ and BiOBr-g-C$_3$N$_4$ is displayed in Fig. 5. The BiOBr and g-C$_3$N$_4$ photocatalysts showed a fundamental absorption edge at 430 nm and 455 nm, respectively. After facets coupling, the BiOBr-g-C$_3$N$_4$ photocatalyst showed the same absorption edge at 455 nm as pure g-C$_3$N$_4$.

The photocatalytic activities for RhB degradation over the investigated samples are shown in Fig. 6a. RhB self-photolysis without catalyst under visible light irradiation is not observable, which indicates that RhB is stable under visible light irradiation. It can be seen that, after 30 min of visible light irradiation, RhB removal over g-C$_3$N$_4$ is as low as 15% and BiOBr also shows a relatively low photocatalytic performance with a degradation ratio of 35%. Significantly, the photocatalytic activity of BiOBr-g-C$_3$N$_4$ displays intensively increases, which induced 95% degradation within 30 min. In order to confirm the significance of facets coupling for the photocatalytic activity of BiOBr-g-C$_3$N$_4$, the directly mixed powders of g-C$_3$N$_4$ and BiOBr with a weight ratio of 1:1 was used. The photodegradation rate of RhB over mixed powders also shows a low photocatalytic performance with a degradation ratio of 25%. It indicates that the enhanced visible-light-driven photocatalytic activity of BiOBr-g-C$_3$N$_4$ comes from the facets coupling.

Fig. 6b showed the PCD percentage of RhB for the initial 30 min of BiOBr with different percents of g-C$_3$N$_4$. It can be found that the best content of g-C$_3$N$_4$ is 50%. Lower or higher content can not obtain the best photocatalytic activity. This optimization content of g-C$_3$N$_4$ is in agreement with reported results about TaON-g-C$_3$N$_4$, [21] TiO$_2$-g-C$_3$N$_4$, [22] and Bi$_2$WO$_6$-g-C$_3$N$_4$, [27] composite photocatalysts. The possible reason is that these composite photocatalysts with 50 wt% g-C$_3$N$_4$ can restrain the recombination of photoinduced charges more effectively [21,22,27].

In order to prove the visible light photocatalytic activity of BiOBr-g-C$_3$N$_4$ comes from the excitation of photocatalyst rather

carbon which was usually observed on the XPS characterization for carbon nitrides. Fig. 4b reveals the N1s spectra. The main N1s peak at 398.5 eV corresponded to sp2 hybridized aromatic N bonded to carbon atoms (C=N—C). The secondly peak at 399.6 eV was assigned to the tertiary N bonded to carbon atoms in the form of N—(C)3 or H—N—(C)2. The thirdly peak with high binding energy at 401.1 eV was attributed to quaternary N bonded three carbon atoms in the aromatic cycles. And the weakest peak at 404.3 eV was assigned to the π-excitations [29,30]. It can be found that no change of chemistry shift appeared except for the disappearing of 404.3 eV for the π-excitations. It implies that the coupling of BiOBr cover up the π-excitations and coupled with g-C$_3$N$_4$ via a interaction using π-electrons of CN heterocycles, rather than coupled with sole C or N atoms of g-C$_3$N$_4$. This result is in agreement with former FR-IR result.
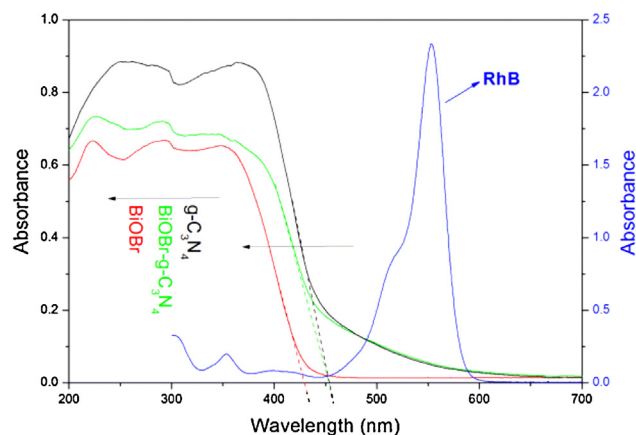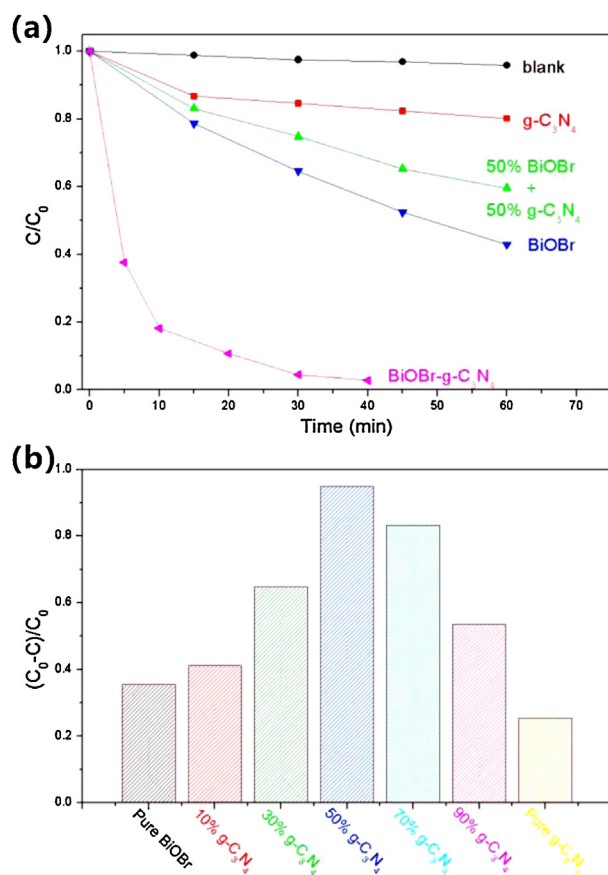
Fig. 6. (a) The PCD percentage of RhB under visible light irradiation ($\lambda \geq 400$ nm); and (b) PCD percentage of RhB for the initial 30 min of BiOBr with different percents of g-C_3N_4.

than the sensitization of RhB, we tested the photocatalytic activity of BiOBr-g-C_3N_4 for RhB degradation with $\lambda \geq 500$ nm irradiation. Fig. 6a showed that, under $\lambda \geq 500$ nm, RhB can be excited but BiOBr, g-C_3N_4 and BiOBr-g-C_3N_4 can not be excited. The little PCD (2.4% for BiOBr, 4.2% for g-C_3N_4, 4.5% for BiOBr-g-C_3N_4) is self-sensitized PCD of RhB as shown in Fig. 7. But, under visible light ($\lambda \geq 400$ nm) irradiation, BiOBr, g-C_3N_4 and BiOBr-g-C_3N_4 can be excited. And there is a high PCD efficiency for these samples (57.2% for BiOBr, 40.5% for g-C_3N_4, 95.5% for BiOBr-g-C_3N_4). It can be found that the self-sensitized PCD is one fortieths of the PCD constant of BiOBr-g-C_3N_4. So, the visible light photocatalytic activity
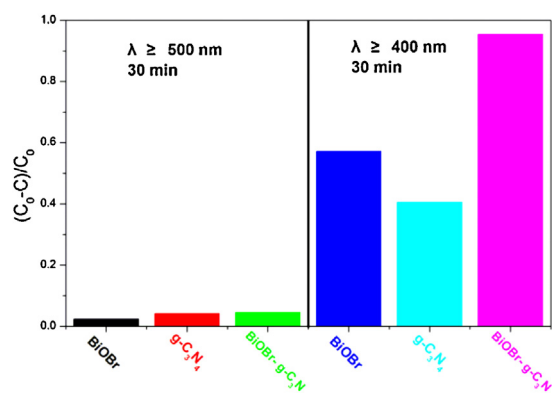

Fig. 7. The PCD percentage of RhB under different visible light irradiation ($\lambda \geq 400$ nm or $\lambda \geq 500$ nm) with 30 min irradiation.
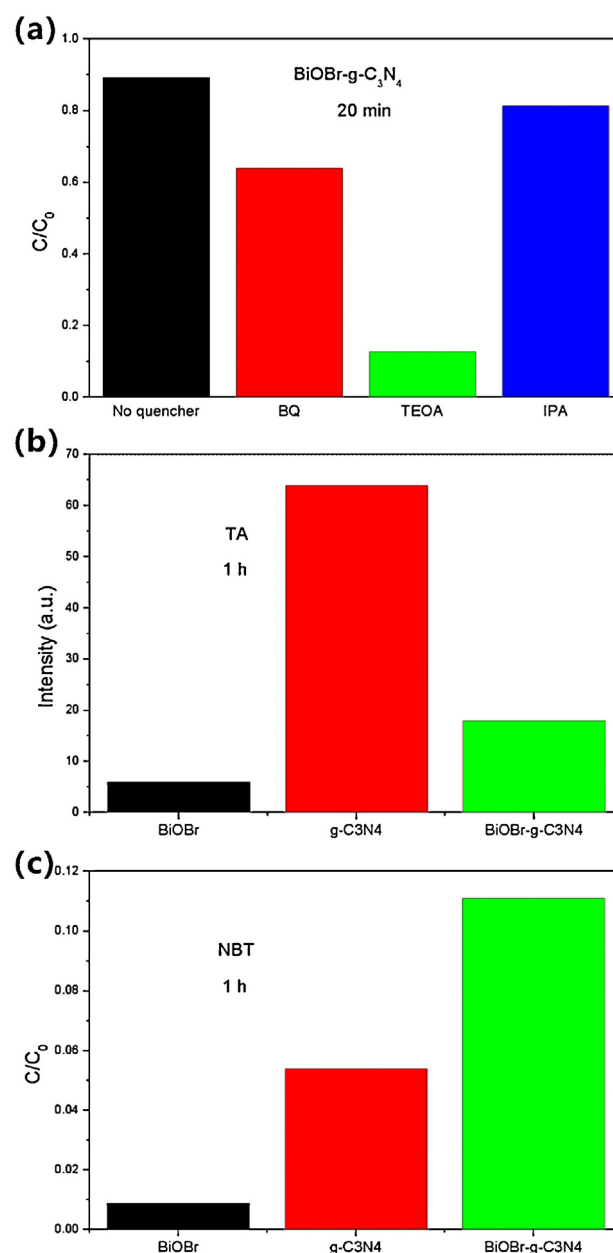

Fig. 8. (a) Trapping experiment of active species during the photocatalytic reaction with 20 min visible light irradiation; (b) fluorescent intensity of TAOH with 1 h visible light irradiation; and (c) transformation percentage of NBT concentration with 1 h visible light irradiation ($\lambda \geq 400$ nm).

of BiOBr-g-C_3N_4 comes from the excitation of photocatalyst rather than self-sensitized PCD of RhB.

3.3. Photocatalytic mechanism

Fig. 8a displays the trapping experiment of active species during the photocatalytic reaction of BiOBr-g-C_3N_4. It can be found that the photocatalytic degradation of RhB was not affected by the addition of 1 mM IPA (a quencher of $^{\bullet}$OH). On the contrary, the photocatalytic degradation of RhB decreased obviously with the addition 1 mM TEOA (a quencher of h+) or 1 mM BQ (a quencher of $O_2^{\bullet}-$). Therefore, it can be concluded that photogenerated holes (h+) and $O_2^{\bullet}-$ are the main active species of BiOBr-g-C_3N_4 for RhB degradation under visible light irradiation [31–37]. For comparison, the trapping experiment of active species during the photocatalytic reaction of mixed powders (50% BiOBr + 50% g-C_3N_4) was tested as
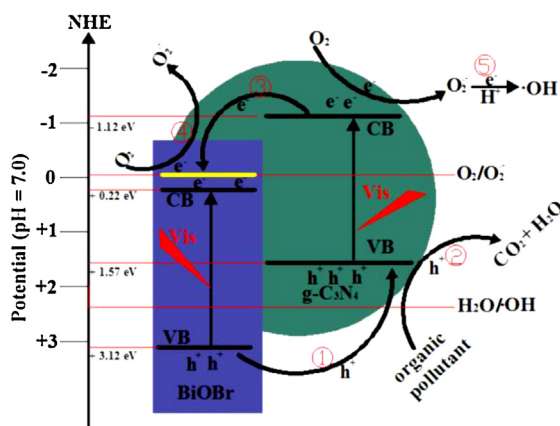
Scheme 2. Photocatalytic mechanism scheme of BiOBr-g-C$_3$N$_4$ under visible light irradiation ($\lambda \geq 400$ nm).

shown in Fig. S4. It can be found that h+, O$_2$•– and •OH are the active species. Obviously, the facets coupling change the photocatalytic mechanism. In order to understand the change of active species after facets coupling between BiOBr and g-C$_3$N$_4$, the detailed O$_2$•– and •OH quantification experiments were used.

Figs. 8b and 7c show the fluorescent intensity of TAOH (quantification experiments of •OH production) and the transformation percentage of NBT (quantification experiments of O$_2$•– production) with 1 h visible light irradiation during the photocatalytic reaction, respectively. For BiOBr, the fluorescent intensity of TAOH and the transformation percentage of NBT can be neglected (Fig. 8b and c). It indicates that there are no •OH and O$_2$•– production from the holes or electrons. The reason is shown as following: the conduction band (CB) potential of BiOBr (0.22 eV vs NHE) is more positive than E$_0$(O$_2$/O$_2$•– = −0.046 eV vs NHE), and the standard redox potential of Bi^{4+}/Bi^{3+} (1.59 eV) [36] is more negative than that of •OH/OH− (+1.99). So, there are no •OH and O$_2$•– production from the holes or electrons.

For g-C$_3$N$_4$, the CB potential of g-C$_3$N$_4$ (−1.12 eV vs NHE) is more negative than E$_0$(O$_2$/O$_2$•– = −0.046 eV vs NHE). Therefore, g-C$_3$N$_4$ shows obviously transformation percentage of NBT (O$_2$•– production). The valence band (VB) potential (1.57 eV vs NHE) is more negative than E$_0$(•OH/OH− = +1.99 eV vs NHE). It indicates that the •OH cannot generate from the h+ in VB of g-C$_3$N$_4$. But, the •OH also can be produced from electrons in CB via a two-electron oxidation pathway [17–20,38]. And previously reports also deemed that •OH come from electrons in CB of g-C$_3$N$_4$ via a two-electron oxidation pathway [17–20,38]. So, the fluorescent intensity of TAOH was very high as shown in Fig. 8c, which reveals the •OH production.

After facets coupling, the fluorescent intensity of TAOH decreased. It indicates that the photogenerated electrons in the CB of g-C$_3$N$_4$ transfer to a higher CB of BiOBr (yellow line in Scheme 2, potential more negative than E$_0$(O$_2$/O$_2$•– = −0.046 eV)) [5,39,40]. Then, there are few remainder electrons in CB of g-C$_3$N$_4$, which result in the decreasing of •OH. And the electrons in the higher CB of BiOBr react with O$_2$ to produce more O$_2$•– (Fig. 8b, the highest transformation percentage of NBT (10.9%) can prove it). On the base of above results, the possible photocatalytic mechanism was shown in Scheme 2.

Under visible light irradiation, both BiOBr and g-C$_3$N$_4$ are excited, and the photogenerated holes and electrons are in their VB and CB, respectively. Then, the internal static electric fields of BiOBr results in that the holes of BiOBr transfer to the interface between BiOBr-{0 0 1} facets and g-C$_3$N$_4$-{0 0 2} facets, and then transfer to the g-C$_3$N$_4$ due to the facets coupling (path 1). At end, the holes oxidize the RhB directly at g-C$_3$N$_4$ surface (path 2). On the other hand, the electrons of g-C$_3$N$_4$ transfer to a higher CB potential

of BiOBr react with O$_2$ to produce increasing O$_2$•– (path 3 and 4). And the remainder electrons in g-C$_3$N$_4$ resulted in the decreasing of •OH (path 5).

3.4. Photocatalytic stability

To test the stability and reusability of the BiOBr-g-C$_3$N$_4$ for the photocatalytic reaction, the catalyst was reused for photocatalytic reaction five times under the same conditions, and the result is shown in Fig. S5. The photocatalytic efficiency of the BiOBr-g-C$_3$N$_4$ decreases only 4% after five cycles. It indicates that the BiOBr-g-C$_3$N$_4$ is stable during the photocatalytic oxidation of the pollutant molecules, which ensures its application.

4. Conclusions

In summary, BiOBr-g-C$_3$N$_4$ inorganic–organic composite photocatalysts were synthesized by a one-step chemical bath method at low temperature. XRD, HRTEM, FT-IR and XPS results revealed that the interreaction between BiOBr and g-C$_3$N$_4$ is facets coupling between BiOBr-{0 0 1} and g-C$_3$N$_4$-{0 0 2}. The facets coupling can result in photoinduced charges transfer between BiOBr and g-C$_3$N$_4$ and enhance the VLD photocatalytic activity for RhB degradation. This research gives a possible explanation for the enhanced photocatalytic activity of inorganic–organic composite photocatalyst.

Appendix A. Supplementary data

Supplementary data associated with this article can be found, in the online version, at http://dx.doi.org/10.1016/j.apcatb.2013.04.058.

References

[1] C. Chen, W. Ma, J. Zhao, Chemical Society Reviews 39 (2010) 4206–4219.
[2] L.W. Zhang, H.B. Fu, Y.F. Zhu, Advanced Functional Materials 18 (15) (2008) 2180–2189.
[3] X. Zhang, Z. Ai, F. Jia, L. Zhang, Journal of Physical Chemistry C 112 (2008) 747–753.
[4] J. Henle, P. Simon, A. Frenzel, S. Scholz, S. Kaskel, Chemistry of Materials 19 (2007) 366–373.
[5] M.A. Gondala, X. Chang, M.A. Ali, Z.H. Yamania, Q. Zhou, G. Ji, Applied Catalysis A-General 397 (2011) 192–200.
[6] L. Ye, J. Liu, C. Gong, L. Tian, T. Peng, L. Zan, ACS Catalysis 2 (2012) 1677–1683.
[7] L. Ye, C. Gong, J. Liu, L. Tian, T. Peng, K. Deng, L. Zan, Journal of Materials Chemistry 22 (2012) 8354–8360.
[8] L. Ye, L. Tian, T. Peng, L. Zan, Journal of Materials Chemistry 21 (2011) 12479–12484.
[9] Y. Feng, L. Li, J. Li, J. Wang, L. Liu, Journal of Hazardous Materials 192 (2011) 538–544.
[10] Y. Fan, Y. Huang, J. Yang, P. Wang, G. Cheng, Environmental Science and Technology 45 (2011) 1593–1600.
[11] J. Xu, W. Meng, Y. Zhang, L. Li, C. Guo, Applied Catalysis B: Environmental 107 (2011) 355–362.
[12] W.L. Huang, Q. Zhu, Computation Materials Science 43 (2008) 1101–1108.
[13] L. Ye, L. Zan, L. Tian, T. Peng, J. Zhang, Chemical Communications 47 (2011) 6951–6953.
[14] J. Jiang, K. Zhao, X. Xiao, L. Zhang, Journal of the American Chemical Society 134 (2012) 4473–4476.
[15] L. Zhang, X.F. Ca, X.T. Chen, Z.L. Xue, Journal of Colloid and Interface Science 354 (2011) 630–636.
[16] D. Zhang, M. Wen, B. Jiang, G. Lia, J.C. Yu, Journal of Hazardous Materials 212 (2012) 104–111.
[17] X. Wang, K. Maeda, A. Thomas, K. Takanabe, G. Xin, J.M. Carlsson, K. Domen, M. Antonietti, Nature Materials 8 (2009) 76–80.

[18] A. Thomas, A. Fischer, F. Goettmann, M. Antonietti, J.O. Muller, R. Schloglb, J.M. Carlsson, Journal of Materials Chemistry 18 (2008) 4893–4908.

[19] G. Liu, P. Niu, C. Sun, S.C. Smith, Z. Chen, G.Q. Lu, H.M. Cheng, Journal of the American Chemical Society 132 (2010) 11642–11648.

[20] X.H. Li, X. Wang, M. Antonietti, Chemical Science 3 (2012) 2170–2174.

[21] S.C. Yan, S.B. Lv, Z.S. Li, Z.G. Zou, Dalton Transactions 39 (2010) 1488–1491.

[22] H. Yan, H. Yang, Journal of Alloys and Compounds 509 (2011) L26–L29.

[23] X. Zhou, F. Peng, H. Wang, H. Yu, Y. Fang, Chemical Communications 47 (2011) 10323–10325.

[24] Y. Wang, R. Shi, J. Lin, Y. Zhu, Energy and Environmental Science 4 (2011) 2922–2929.

[25] J.X. Sun, Y.P. Yuan, L.G. Qiu, X. Jiang, A.J. Xie, Y.H. Shen, J.F. Zhu, Dalton Transactions 41 (2012) 6756–6763.

[26] Y. Wang, X. Bai, C. Pan, J. He, Y. Zhu, Journal of Materials Chemistry 22 (2012) 11568–11573.

[27] L. Ge, C. Han, J. Liu, Applied Catalysis B 109 (2011) 100–107.

[28] X. Xu, G. Liu, C. Randorn, J.T.S. Irvine, International Journal of Hydrogen Energy 36 (2011) 13501–13507.

[29] G. Zhang, J. Zhang, M. Zhang, X. Wang, Journal of Materials Chemistry 22 (2012) 8083–8091.

[30] J. Liu, T. Zhang, Z. Wang, G. Dawson, W. Chen, Journal of Materials Chemistry 21 (2011) 14398–14401.

[31] G. Li, K.H. Wong, X. Zhang, C. Hu, J.C. Yu, R.C.Y. Chan, P.K. Wong, Chemosphere 76 (2009) 1185–1191.

[32] Y. Chen, S. Yang, K. Wang, L. Lou, Journal of Photochemistry and Photobiology A 172 (2005) 47–54.

[33] P. Ji, J. Zhang, F. Chen, M. Anpo, Applied Catalysis B 85 (2009) 148–154.

[34] M. Yin, Z. Li, J. Kou, Z. Zou, Environmental Science and Technology 43 (2009) 8361–8366.

[35] A.N. Rao, B. Sivasankar, V. Sadasivam, Journal of Molecular Catalysis A 306 (2009) 77–81.

[36] H. Fu, C. Pan, W. Yao, Y. Zhu, Journal of Physical Chemistry B 109 (2005) 22432–22439.

[37] T. Xu, L. Zhang, H. Cheng, Y. Zhu, Applied Catalysis B 101 (3) (2011) 382–387.

[38] Y. Cui, J. Huang, X. Fu, X. Wang, Catalysis Science and Technology 2 (2012) 1396–1402.

[39] X. Zhang, L. Zhang, T. Xie, D. Wang, Journal of Physical Chemistry C 113 (2009) 7371–7378.

[40] L. Ye, J. Chen, L. Tian, J. Liu, T. Peng, K. Deng, L. Zan, Applied Catalysis B 130–131 (2013) 1–7.